Petroleum Research 11 (2026) 1021–1036

Contents lists available at ScienceDirect

Petroleum Research

journal homepage: http://www.keaipublishing.com/en/journals/petroleum-research/

Full Length Article

Inversion method for multi-section friction factors in horizontal wells based on Fisher optimal segmentation and SSA

Hu Yin [a], Qianyi Xia [a,*], Qiang Wei [b], Xiuwen Zhao [a], Qian Li [a]

[a] Petroleum Engineering School, Southwest Petroleum University, Chengdu, 610500, China
[b] Chuanxi Drilling Company, CNPC Chuanqing Drilling Engineering Company Limited, Chengdu, 610051, China

ARTICLE INFO

Article history:
Received 20 August 2025
Received in revised form
13 January 2026
Accepted 15 January 2026
Available online 22 January 2026

Keywords:
Friction factor
Drag and torque
Inverse analysis
Fisher optimal segmentation
Sparrow search algorithm

ABSTRACT

The friction factor plays a critical role in drag and torque calculations. In the drag and torque model, the friction factor is typically treated as an average value, or the wellbore is roughly divided into casedhole and openhole segments with different values assigned. Such simplified model parameters fail to account for variations in the friction factor across different well segments, impacting the accuracy of the computations. Precise drag and torque calculations are significant, and the prerequisite for accurate drag prediction is the inverse analysis of realistic friction factor parameters. This study proposes a friction factor inverse analysis method based on morphological characteristics of measured data. The Fisher optimal segmentation method is employed to divide the field-measured data into multiple reasonable subsegments based on curve morphology features, indirectly determining the segmentation of the friction factor. The 3D stiff-string drag and torque model is used to establish friction factors inverse model, with corresponding friction factors introduced separately for the segmented well sections. The sparrow search algorithm, enhanced by opposition-based learning strategy, is utilized to optimize the segmented friction factors, with the optimization evaluation criteria simultaneously assessing the deviation and similarity between simulated and actual curves. Case studies demonstrate that the friction factor inverse analysis method proposed in this study, leveraging the curve morphology features of real-time drilling data, can efficiently obtain high-precision segmented friction coefficients. This method significantly reduces the error between simulated and field-measured data, improving calculation accuracy by about 50%, thus providing robust data support for accurate drag and torque prediction. Furthermore, the division approach can be applied during a round trip to optimize drilling parameters, enhancing the efficiency of drilling parameter control.

© 2026 Chinese Petroleum Society. Publishing services by Elsevier B.V. on behalf of KeAi Communications Co. Ltd. This is an open access article under the CC BY-NC-ND license (http://creativecommons.org/licenses/by-nc-nd/4.0/).

1. Introduction

Drag and torque pose significant challenges in drilling operations, with their accurate control being an important direction of current research. The value of the friction factor is a key factor in analyzing wellbore drag and torque. The inversion of the friction factor generally involves two strategies: single-value inversion and general segmented inversion. The single-value inversion strategy utilizes multiple measured points, independently setting the friction factor for each measured point to perform the inversion. This method assumes that when the bit reaches a certain depth, the friction factor along the drillstring is a constant, relying on calculations at multiple well depths to obtain this parameter for the entire wellbore. Although this approach can analyze the relative variation trend of the drag through multiple inversions, it overlooks the differences in drag and torque contributions from various well sections, yielding an averaged friction factor. The second, more commonly used general segmented strategy involves dividing the wellbore into open and cased holes for separate inversion. This division approach fails to fully reflect the complex variations in drag and torque within the open hole. The oversimplified results of the general segmented method lead to poor correlation between predicted surface torque values or hookloads and actual data.

In the 1980s, with the emergence of extended-reach horizontal wells, drag and torque issues gradually emerged and gained

* Corresponding author.
E-mail address: sia_0109@163.com (Q. Xia).
Peer review under the responsibility of Editorial Office of Petroleum Research.

https://doi.org/10.1016/j.ptlrs.2026.01.008
2096-2495/© 2026 Chinese Petroleum Society. Publishing services by Elsevier B.V. on behalf of KeAi Communications Co. Ltd. This is an open access article under the CC BY-NC-ND license (http://creativecommons.org/licenses/by-nc-nd/4.0/).

Nomenclature

e_t, e_n, e_b	Unit base vector in natural curvilinear system, dimensionless
α	Inclination angle, *rad*
φ	Azimuth angle, *rad*
C_{f1}, C_{f2}	Axial and circumferential friction factors, dimensionless
D_t	Outer diameter of the pipe, m
EI	Bending stiffness, $N{\cdot}m^2$
k_b	Wellbore curvature, $rad{\cdot}m^{-1}$
k_n	Wellbore torsion, $rad{\cdot}m^{-1}$
k_f	Buoyancy factor, dimensionless
M_t	Drillstring torque, $N{\cdot}m$
M_b	Bending moment, $N{\cdot}m$
M_0	Surface torque, $N{\cdot}m$
M_{tob}	Bit torque, $N{\cdot}m$
N	Distributed normal contact force, in the e_n and e_b directions, $N{\cdot}m^{-1}$
N_n, N_b	Components of N in e_n and e_b directions, respectively, $N{\cdot}m^{-1}$
Q_n, Q_b	Components of shear force in e_n and e_b directions, respectively, $N{\cdot}m^{-1}$
q_c	Distributed contact force vector on drillstring, $N{\cdot}m^{-1}$
q_m	Weight per unit length, $N{\cdot}m^{-1}$
T	Actual axial tension, N

attention. After years of research, drag and torque calculation models have become relatively mature, primarily categorized into soft-string and stiff-string models. The soft-string model was first proposed by Johancsik et al. (1984) and converted into differential equation form by Sheppard et al. (1987). This model has low computational complexity and is widely applied in drag and torque calculations. The standard soft-string model, by ignoring stiffness, exhibits deviations in predicted results when calculating the drill collar and high dogleg severity sections. Aadnoy et al. (2010) provided distinct modeling equations for straight and curved wellbore sections to address this limitation. Ho (1988) and subsequent researchers, including Mitchell and Samuel (2009) and Mirhaj et al. (2016), emphasized that shear force and bending stiffness are key to ensuring the reliability of drag and torque models. On these bases, the stiff-string model has been further improved, incorporating the radial clearance between wellbore and drillstring (Tikhonov et al., 2014), the influence of bow spring centralizers (Dao et al., 2023), and the effect of cuttings transport (Zhao et al., 2024). Modern technologies have also been extensively employed in drag and torque analysis. Carpenter (2021) leveraged digital transformation to integrate soft-string and stiff-string models with the Real-Time Drilling (RTD) system, achieving automated real-time torque-and-drag (RT-T&D) analysis. Mayouf and Hadjadj (2024) showcased the application potential of various machine learning models in real-time hook load prediction.

Key parameters of classical drag and torque models include drillstring weight, wellbore tortuosity, and friction factors. Although existing models vary in form, their structural differences have a less significant impact on computational accuracy compared to the influence of friction factors. Accurate calculation of drag and torque is the basis for monitoring downhole conditions, and obtaining an accurate and realistic friction factor is a prerequisite for precise drag and torque calculations. The friction factor is essentially a cumulative parameter that is unwillingly influenced by wellbore tortuosity, formation properties, type of mud and lubricity, and temperature (Samuel, 2010; Wiktorski et al., 2020). When the bit depth reaches a certain well depth, the field data available are typically restricted to surface torque values and hookloads. The friction factor must be derived through inversion due to insufficient measured data along the drillstring. Subsequently, load distribution at arbitrary positions of the drillstring can be obtained via forward simulation of the friction factor. To simplify calculations, single-value or general segmented friction factor settings are commonly adopted, and this approach is broadly utilized in the model calibration, parameter predictions, and stuck pipe detection. However, the failure to consider variations in the friction factor across openhole sections may introduce some error into calculations.

Craig (2003) attempted to analyze the forces on coiled tubing using a single-value friction coefficient. However, he suggested that engineers should use varying friction coefficients in complex well completions to account for different tubular types. Hareland et al. (2014) and Tahmeen et al. (2014) achieved downhole weight on bit (DWOB) prediction by adjusting parameters such as the friction coefficient to align simulated DWOB with actual values. Lai et al. (2016) appropriately reduced the casing friction factor to match predicted pick-up (PU) and slack-off (SO) weights to measurements, eliminating discrepancies and demonstrating the friction factor's capability to calibrate the model. Tang et al. (2016) proposed a method for analyzing downhole drag and torque in extended-reach wells during drilling, using real-time hookloads to adjust the friction coefficient, enabling the evaluation of drillstring conditions and optimization of drilling parameters. Zhao et al. (2022) inverted for friction factors on cased and open-hole sections, adjusting the weight function related to well depth to assess long-term, short-term, and real-time operation risks. Samuel and Kumar (2023) assessed casing runnability by decomposing the friction factor in real time. Leveraging intelligent algorithms, recent studies have adopted a unified friction factor to characterize drag across entire well sections, dynamically calibrating the friction factor through Bayesian optimization or neural networks, and predicting stuck pipe risks by monitoring abnormal friction (Chi et al., 2023; Zhu et al., 2021).

Studies have sought precise friction factors by dividing the wellbore into multiple segments to enhance the accuracy of friction factor inversion. Chen et al. (2015) pioneered this method, dividing the wellbore into multiple sections based on wellbore geometry and assigning corresponding friction factors to each segment. Qin et al. (2022) employed clustering algorithms to process pre-drilling data for wellbore segmentation, this method performs relatively stably during the process of tripping or casing running, but faces challenges in data collection.

This study proposes a multi-section friction factors inversion method for horizontal wells. The Fisher optimal segmentation method applies to divide the wellbore into segments from the wellhead downward based on the curve morphology features of actual hookloads or surface torque values, and to assign a specific friction factor to each subsegment. The optimal segmented friction factors are obtained by minimizing the objective function through the opposition-based learning strategy enhanced sparrow search algorithm. All wellbore sections undergo simultaneous inversion, with their friction factors mutually influencing each other. Segmented friction factors provide detailed drag information, enabling drillers to effectively monitor downhole conditions during a round trip and optimize drilling parameters.

2. 3D stiff-string drag and torque model

In the 3D stiff-string model (Ho, 1988), Variations in both well inclination and azimuth induce bending characteristics along the drillstring element, resulting in a three-dimensional curve. The forces acting on the drillstring element constitute a spatial force system, for which a Cartesian coordinate system is established, as shown in Fig. 1. In the coordinate system, the origin O is positioned at the wellhead, with the N axis pointing to the north, and the unit vector is $\vec{i}$; the E axis points to the east, and the unit vector is $\vec{j}$; the D axis points to the vertical direction, and the unit vector is k. A point O' on the wellbore axis is chosen to establish the natural coordinate system, where e_t is the unit vector in the tangent direction of the wellbore axis, e_n is the unit vector in the principal normal direction, and e_b is the unit vector in the binormal direction.

The stiff-string model assumes continuous contact between the drillstring and the wellbore, with its centerline conforming to the wellbore trajectory. This model accounts for drillstring stiffness, permitting bending-induced deformation while neglecting torsional and shear deformations. The buoyant weight, normal contact force, and frictional force acting on a differential segment are continuously distributed along its length. The model is static, neglecting dynamic behaviors such as drillstring vibration. It assumes non-zero bending moments and shear forces at pipe cross-sections. The drillstring is discretized into multiple elements, with distributed contact forces determined iteratively using the superposition principle. Force analysis of the drillstring unit AB is conducted, as illustrated in Fig. 2. The torque and drag stiff-string model formulation is given in Equation (1).

$$\begin{cases} \dfrac{d}{ds}\left(T+\dfrac{M_b^2}{2EI}\right) = q_m k_f \cos\alpha \pm C_{f1}N \\ N_n = \dfrac{d^2M_b}{ds^2} - k_b T - k_n(k_b M_t + k_n M_b) - q_m k_f\left(\dfrac{1}{k_b}\dfrac{d\alpha}{ds}\sin\alpha\right) \\ N_b = \dfrac{d}{ds}(k_b M_t + k_n M_b) + k_n\dfrac{dM_b}{ds} + q_m k_f\left(\dfrac{1}{k_b}\dfrac{d\varphi}{ds}\sin^2\alpha\right) \\ \dfrac{dM_t}{ds} = \dfrac{C_{f2}ND_t}{2} \\ N^2 = N_n^2 + N_b^2 \end{cases} \tag{1}$$

The basic steps of the friction factor inversion involve iterative calculations and error assessment. The conventional friction factor inversion method first assumes an initial friction factor based on empirical values, then incorporates parameters including wellbore trajectory, drillstring assembly, and mud properties into the torque and drag model for calculation. The model divides the wellbore into multiple elements, and the axial loads and torque are iteratively calculated from the bottom hole to the surface, ultimately generating simulated hookload and surface torque at the wellhead. The simulated value is then compared with the measured data at corresponding depths for error evaluation. If the error exceeds the predefined accuracy threshold, the friction factor is adjusted, and iterative calculations are repeated until the desired accuracy is achieved. Ultimately, the ideal friction factor is obtained. The key to inversion lies in adjusting the friction factor to minimize the discrepancy between simulated and measured data.

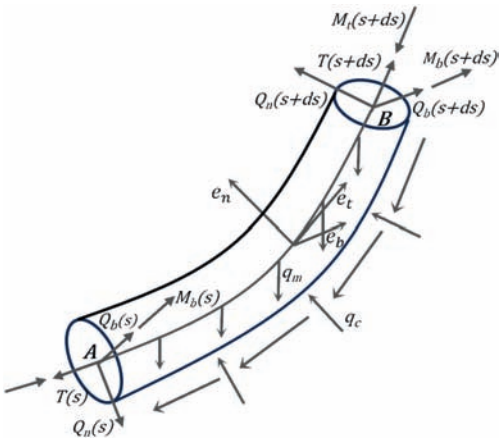


Fig. 2. Force analysis diagram of the drillstring unit AB.

3. Well section division

3.1. Curve characteristics-based segmentation

Dividing the horizontal wellbore into multiple sections and assigning corresponding friction factors is illustrated in Fig. 3. Previous methods for tripping or casing running operations generally depended on manual segmentation or clustering of pre-drilling data to divide the wellbore into segments. Manual segmentation is heavily dependent on human expertise and lacks a unified scientific foundation, whereas clustering results are predominantly influenced by the quality and completeness of input data.

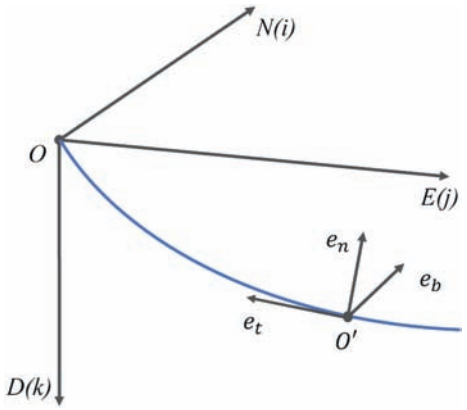


Fig. 1. Establishing the coordinate system.

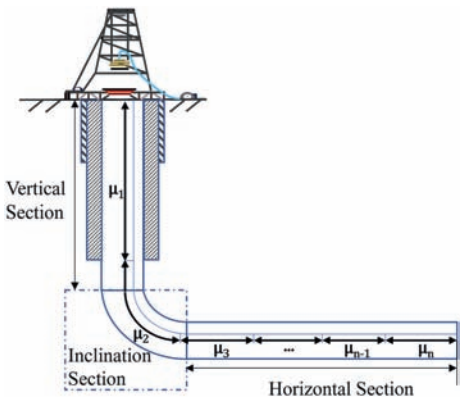


Fig. 3. Schematic of well sections division.

This study proposes a wellbore segmentation approach based on measured data, since these measurements indirectly reflect the combined effects of multiple uncertain factors—including drillstring-wellbore contact, wellbore curvature, and formation properties—on drag and torque. Consequently, segmenting measured curves is of significant value as it accurately identifies local variations in downhole drag. The primary advantage of this new method stems from its ability to select specific depth intervals for focused analysis, which allows for more targeted evaluations. In comparison, previous segmentation methods generally partition the entire well from wellhead to total depth without adaptability for specific intervals.

This study employs the Fisher optimal segmentation method to identify hookload or torque measurements' curve morphology features, thereby determining friction factors' segmentation. Based on field-collected data, measured hookloads F_{hk} and surface torque T_{tq} at various depths are gathered, which can be represented as the following vectors:

$$F_{hk} = \left[F_{hk_1}, F_{hk_2}, \cdots, F_{hk_n} \right]^T \tag{2}$$

$$T_{tq} = \left[T_{tq_1}, T_{tq_2}, \cdots, T_{tq_n} \right]^T \tag{3}$$

Fluctuations and noise in F_{hk} and T_{tq} compromise subsequent segmentation tasks. The Savitzky-Golay filter (Savitzky and Golay, 1964) is applied for data smoothing and noise reduction.

3.2. Fisher optimal segmentation method

The Fisher optimal segmentation method (Fisher, 1958; Lindberg, 1990) is a clustering algorithm designed to split time series samples without disrupting the order of sequence samples. This algorithm aims to minimize intra-class variance while preserving inter-class differences. There are n time series samples, with p indicators measured for each sample. The original data matrix is represented as:

$$\underset{(p\times n)}{X} = \begin{bmatrix} x_{11} & x_{12} & \cdots & x_{1n} \\ x_{21} & x_{22} & \cdots & x_{2n} \\ x_{31} & x_{23} & \cdots & x_{2n} \\ \cdots & \cdots & \cdots & \cdots \\ x_{p1} & x_{p2} & \cdots & x_{pn} \end{bmatrix} \tag{4}$$

The element x_{ij} denotes the observed value of the i indicator for the j th sample. Generally, the variability within a segment is quantified by the sum of squared deviations (SSD). However, SSD assumes time series data stationarity and performs poorly when significant trends exist. Hookloads and surface torque values show a consistent increasing or decreasing trend. In drilling operations, simulated curves exhibit a consistent varying trend, rendering simple mean calculations ineffective. Thus, SSD alone degrades segmentation accuracy. This paper replaces the traditional SSD approach with the residual sum of squares (RSS) to address this issue. For a cluster $Q = \left\{ x_i, x_{i+1}, \ldots, x_j \right\} (j > i)$, the samples are partitioned into k consecutive segments. After fitting the samples in each segment using the least squares method, the residuals of each sample relative to the corresponding fitted line are calculated. Smaller residuals indicate greater consistency within the segment. The fitted line for each segment is expressed as $\beta_0 + \beta_1 x$ to minimize the RSS for the samples within the segment. The consistency within a segment is measured by its "diameter", which is determined by calculating the RSS for all samples within that segment. Let $D(i,j)$ represent the diameter of Q, and its calculation formula is as follows:

$$D(i,j) = \sum_{i}^{j} \left(y_k - (\beta_0 + \beta_1 x_k) \right)^2 \tag{5}$$

Where x_k represents the label of the k sample (e.g., time, depth), and y_k represents the observed value of the k sample. $\beta_0 + \beta_1 x_k$ denotes the fitted value of the k sample, corresponding to the predicted value of the linear model. The algorithm defines an objective function $B(n,k)$, representing the sum of the "diameters" of all segments to optimize clustering.

$$B(n,k) = \sum_{t=1}^{k} D(i_t, i_{t+1} - 1) \tag{6}$$

The Fisher optimal segmentation method identifies the optimal segmentation points by minimizing the value of the objective function, $B^*(n,k)$, which serves as the algorithm's core.

$$B^*(n,k) = min \sum_{t=1}^{k} D(i_t, i_{t+1} - 1) \tag{7}$$

The algorithm adopts a dynamic programming strategy. It first optimizes for the case of $k = 2$ and gradually increases the number of segments k. Specifically, it iterates through all possible segmentation points $i \in (1, n-1)$ and calculates $B(n,2)$ corresponding to each potential point. Finally, the point with the minimum $B(n,2)$ is selected as the optimal segmentation point i_1, thereby obtaining the segmentation scheme corresponding to $B^*(n,2)$. Subsequently, a new segment is added to the optimization result of the previous step each time until the preset final number of segments k is reached. The new segment is added by iterating through all possible new segmentation points based on the previous optimal segmentation, and the scheme with the minimum total residual is identified. This stepwise incremental approach ensures that each intermediate step is as close as possible to the optimal solution. After the calculation, the positions of all segmentation points are determined through backtracking: the last segmentation point i_k is known to minimize the objective function $B^*(n,k)$; then backtracking sequentially forward to find the segmentation point i_{k-1} that minimizes $B^*(i_{k-1}, k-1)$, and so on, ultimately determining the positions of all segmentation points. The recursive formula is as follows:

$$\begin{cases} B^*(n,2) = min_{2\le i\le n}\{B(1,i-1) + D(i,n)\} & k = 2 \\ B^*(n,k) = min_{k\le i\le n}\{B(i-1,k-1) + D(i,n)\} & k > 2 \end{cases} \tag{8}$$

The maximum number of segments is determined by the requirement that the average segment length in the wellbore is at least 300 m. For the dynamic determination of the target number of segments, this paper defines a *Threshold* using the error retention ratio to judge whether the contribution of error reduction from adding a new segment is significant, with a reference value range of $[0.7, 0.9]$. The more segments there are, the smaller the total residual. The ratio $B(n,k)/B(n,k-1)$ can represent the error retention ratio when increasing the number of segments from $k-1$ to k. When the error retention ratio is less than the threshold, the contribution of error reduction from the new segment is significant, and segments should continue to be added; conversely, when the error reduction rate is insufficient, segment addition is stopped, and $k-1$ is the effective number of segments under the current threshold. The pseudocode for the wellbore segment

division process is shown in Appendix Algorithm 1. The *Threshold* formula is as follows:

$$Threshold \leq \frac{B(n,k)}{B(n,k-1)} \tag{9}$$

It should be noted that $[0.7, 0.9]$ is a conventional value range rather than an absolute constraint. The sensitivity analysis in Fig. 4 for segmenting 1500 m and 3000 m wellbore sections shows that thresholds below 0.7 impose stringent error reduction requirements, resulting in only 1–2 segments per section; if the threshold is close to or higher than 0.9, it tends to approach the upper limit of the number of segments. The $[0.7, 0.9]$ range can provide a variety of moderate segmentation schemes, enabling flexible division of segments according to actual needs. When high-precision friction factors are required for calculation, a threshold of approximately 0.85 can be selected; if calculation efficiency is prioritized, a threshold of around 0.7 is recommended to shorten the subsequent inversion time. This range is particularly suitable for the segmentation of long wellbore sections, balancing the rationality of the method and engineering operability.

3.3. Equivalent processing method for hookload offset caused by pumping

It is clarified that the drilling team does not pump drilling fluid in real time during tripping-in. Due to the effects of buoyancy and the empty drill string, tripping-in friction may appear relatively high. Drilling fluid is typically pumped only at fixed depth intervals or appropriate points, after which the drillstring friction factor returns to normal. Based on this on-site scenario, two processing strategies are adopted for wellbores with different mud-filling effect.

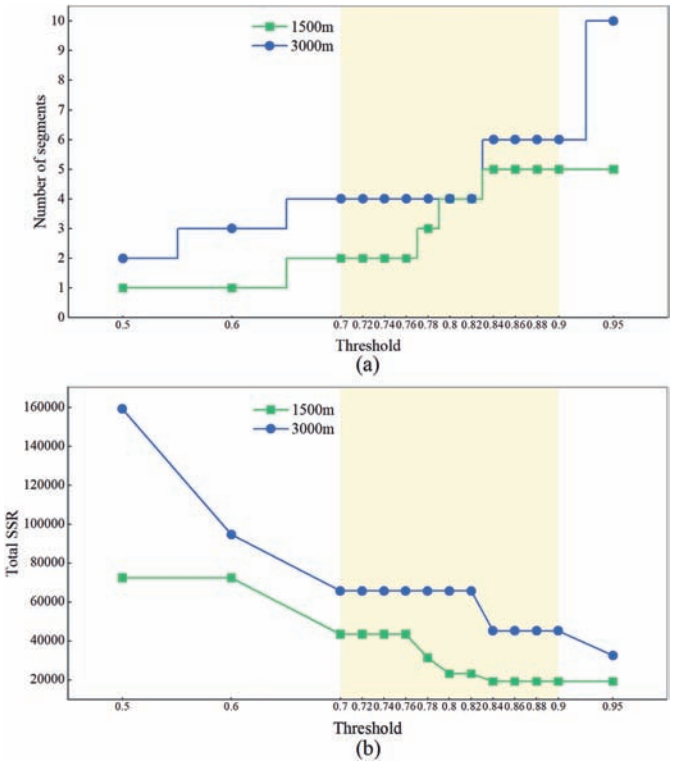


Fig. 4. Sensitivity analysis of threshold (a) Relationship between threshold and number of segments (b) Relationship between threshold and SSR.

3.3.1. Wellbores with insignificant mud-filling effects

For such wellbores, the hookload curve is less affected by mud-filling. Additionally, we perform SG filtering preprocessing on the data prior to wellbore section segmentation. This filtering mitigates the interference caused by mud-filling, thereby reducing the likelihood of misidentifying mud-filling offset points as segmentation boundaries to some extent. Therefore, segmented inversion can be directly conducted for such cases.

3.3.2. Wellbores with significant mud-filling effects

For instance, taking the S1 well case as an example for analysis, its hookloads during tripping-in is shown in Fig. 5. The processing workflow involves first identifying mud-filling points, followed by zonal processing to equate discontinuous mud-filling to continuous mud-filling. For such wellbores, obvious hookload drift occurs during discontinuous mud-filling; this characteristic is highly suitable for identifying mud-filling points using the Fisher optimal segmentation method..

(1) **Identification of discontinuous pumping points.** Mud-filling operations should be performed at set intervals, but due to factors such as on-site operational pace, deviations exist in the actual depth distribution of mud-filling points. Therefore, the collected data are grouped into sets of 30 points each, with the mean value of each group calculated as a sample point. The Fisher optimal segmentation algorithm is applied to hookloads of the entire wellbore section, as shown in Fig. 6, to accurately identify the segmentation points (i.e., mud-filling points). Each segmentation segment corresponds to one mud-filling operation, and the mud-filling depths and corresponding hookload values are presented in Table 1.

(2) **Equivalent continuous mud-filling treatment for open-hole sections.** In cases of discontinuous mud-filling in open-hole sections, equivalence between the hookload under discontinuous and continuous mud-filling is achieved by adding the weight of drilling fluid to the actual hookload values. Using the identified mud-filling points as boundaries, the entire wellbore section is divided into several mud-filling interval segments, ensuring that the upper and lower boundaries of each interval segment are two adjacent discontinuous mud-filling points. Subsequently, each interval segment is subdivided into small segments every 30 m. The contribution value of drilling fluid weight is calculated based on the basic parameters for each small segment. The weight contribution values of all small segments within the same mud-filling interval segment up to the current depth are then summed to obtain the hookload compensation value for that depth relative to the previous mud-filling point. Superimposing this compensation with original hookloads yields the desired equivalent hookload curve, as shown in Fig. 7.

(3) **Segmentation of the open-hole section.** Based on the obtained equivalent continuous mud-filling hookloads, the Fisher optimal segmentation method is applied again to divide the section into segments, as shown in Table 2. Since the equivalent hookload has eliminated the interference from discontinuous mud-filling, the segmentation boundaries can remain unaffected by pumping operations. In the final inversion, original discontinuous mud-filling hookloads are still used for the optimization, ensuring that the inversion results align correctly with on-site actual hookloads.

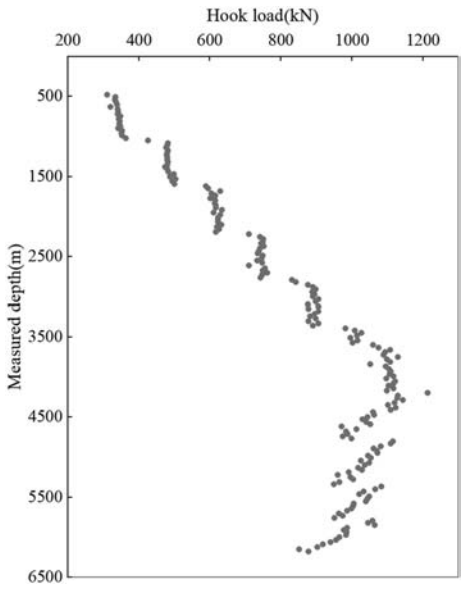


Fig. 5. Hookload offset phenomenon induced by discontinuous mud-filling.

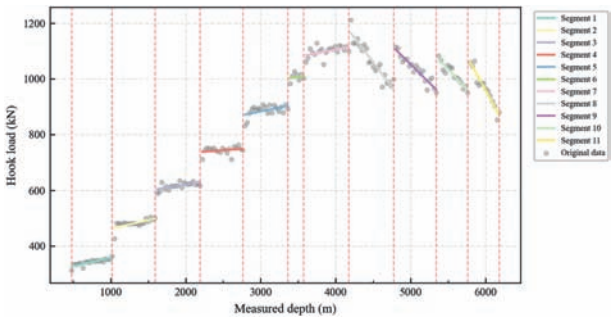


Fig. 6. Identification of well sections without mud-filling.

4. Intelligent inversion approach for friction factors

4.1. Improved sparrow search algorithm

The Sparrow Search Algorithm (SSA) (Xue and Shen, 2020) imitates the foraging and anti-predation behaviors of sparrows to perform optimization through local and global search strategies. On single-peak and multi-peak benchmark functions, SSA outperforms traditional algorithms like Particle Swarm Optimization (PSO) as well as novel algorithms such as Gray Wolf Optimizer (GWO).

Individuals in the sparrow population are classified into two distinct roles: producers and scroungers. An early-warning mechanism is introduced, with some sparrows taking on vigilance tasks. Producers provide foraging areas and directions for the entire population, typically possessing higher energy levels (higher fitness). Scroungers continuously follow producers to obtain food, thereby enhancing their predation efficiency. Roles within the population are dynamic, allowing sparrows to alternate flexibly between producer and scrounger behaviors. When danger is detected, sparrows at the edge of the group quickly move to safer areas to secure more advantageous positions, while those in the center randomly move.

4.1.1. Sparrow algorithm update rules

Each sparrow's position in the SSA represents a solution in the solution space. Assuming a population of n sparrows, the fitness values of the sparrow population can be represented as follows:

$$F_X = \begin{bmatrix} f([x_{1,1} & x_{1,2} & \cdots & x_{1,d}]) \\ f([x_{2,1} & x_{2,2} & \cdots & x_{2,d}]) \\ & \vdots & & \\ f([x_{n,1} & x_{n,2} & \cdots & x_{n,d}]) \end{bmatrix} \tag{10}$$

Where f denotes the fitness value, and d represents the dimension. Since producers guide the movement of the entire population, they search in a broader foraging range. In each iteration, the location of producers is updated as follows:

$$X_{i,j}^{t+1} = \begin{cases} X_{i,j}^{t} \cdot exp\left(-\dfrac{i}{\alpha \cdot iter_{max}} \right) & if \;\; R_2 < ST \\ X_{i,j}^{t} + Q \cdot L \;\; if \;\; R_2 \geq ST \end{cases} \tag{11}$$

Where t represents the current iteration number, and $j = 1,2,3,\ldots,d$. $item_{max}$ is a constant specifying the maximum allowable iterations, and X_{ij} indicates the position of the i sparrow in the j th dimension. $R_2 (R_2 \in (0,1])$ and $ST (ST \in [0.5,1])$ represent the alarm value and safety threshold, respectively. Q is a random variable following a normal distribution, and $\alpha \in (0,1]$ is a random coefficient. L denotes a $1 \times d$ matrix with all elements equal to 1. When $R_2 < ST$, it indicates that few predators are nearby, allowing producers to conduct global foraging. If $R_2 \geq ST$, it suggests that some sparrows in the population have detected predators, prompting producers to execute random movement based on a normal distribution to avoid them.

Scroungers continuously monitor the behavior of producers. When they detect better food sources from a producer, they immediately move toward the producer's position. The position of scroungers is updated as follows:

$$X_{i,j}^{t+1} = \begin{cases} Q \cdot exp\left(\dfrac{X_{\text{worst}} - X_{i,j}^{t}}{i^2} \right) & if \quad i > n/2 \\ X_p^{t+1} + \left| X_{i,j}^{t} - X_p^{t+1} \right| \cdot A^{+} \cdot L & \text{otherwise} \end{cases} \tag{12}$$

Where X_p represents the producer's best-found location, and X_{worse} refers to the least optimal position at present. A is a $1 \times d$ matrix with each element randomly assigned a value of 1 or -1, with $A^{+} = A^{T}\left(AA^{T}\right)^{-1}$. When $i > n/2$, it indicates that the i scrounger, with a low fitness value, has failed to secure resources and is experiencing extreme hunger. In this case, the scrounger must change its foraging direction to find more resources.

The location update of sparrows that are aware of danger can be expressed as follows:

$$X_{i,j}^{t+1} = \begin{cases} X_{best}^{t} + \beta \cdot \left| X_{i,j}^{t} - X_{best}^{t} \right| & if \;\; f_i > f_g \\ X_{i,j}^{t} + K \cdot \left(\dfrac{\left| X_{i,j}^{t} - X_{worst}^{t} \right|}{(f_i - f_w) + \varepsilon} \right) & if \;\; f_i = f_g \end{cases} \tag{13}$$

Where X_{best} represents the current global best position. The step size control parameter β is a random number following a normal distribution with a mean of 0 and a variance of 1. $K \in [-1,1]$ is a random number used to denote the direction of sparrow movement. It serves as the step size control parameter. f_i denotes the fitness value of the current sparrow individual, while f_g and f_w correspond to the global best and worst fitness values,

Table 1
Mud-filling points.

No.	Depth [m]	Hookload [kN]	No.	Depth [m]	Hookload [kN]	No.	Depth [m]	Hookload [kN]
1	480.00	311.3	5	2790.27	831.28	9	4800.02	1115.96
2	1050.41	426.22	6	3390.01	982.87	10	5370.08	1082.7
3	1620.23	588.8	7	3600.52	1060.49	11	5790.45	1058.7
4	2220.77	710.51	8	4200.62	1212.76	12	6150.04	852.39

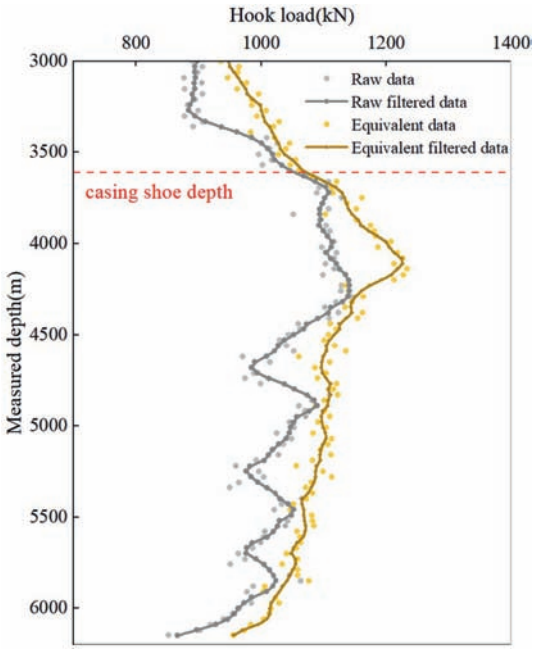


Fig. 7. Equivalent hookload curve for simulated continuous mud-filling.

Table 2
Segmentation results of open-hole section in Well S1.

No.	Well sections [m]	Friction factors
1	3612–4110	μ_1
2	4110–4500	μ_2
3	4500–5041	μ_3
4	5041–6060	μ_4
5	6060–6150	μ_5

respectively. ε is a small constant used to prevent invalid calculations.

4.1.2. Opposition-based learning strategy

The opposition-based learning (OBL) strategy (Tizhoosh, 2005) aims to expand the search space by generating and comparing its opposite solution with the current solution. For a given initial solution, OBL calculates its opposite solution in the search space and evaluates the optimal one from both solutions. Integrating the OBL strategy into SSA expands the search range and increases the potential for finding the global optimum (Gharehchopogh et al., 2023).

The concept of elite individuals is introduced to reduce resource waste caused by the randomness of OBL. In this study, the top 10% of sparrows, ranked by fitness, are identified as elite solutions before updating the positions of the sparrows. These elite solutions define dynamic boundaries based on their positional information. Subsequently, the OBL strategy is applied to calculate the opposite solutions. By comparing the fitness values of individuals before and after the update, the current individual replaces the previous one if its fitness is better. Let $x_i(t)$ denote a solution at iteration t, and its opposite solution be $x_i(t)'$. Let $f(x)$ represent the objective function. If $f(x_i(t)) \geq f(x_i(t)')$, then $x_i(t)$ is referred to as the elite individual at iteration t; if $f(x_i(t)) \leq f(x_i(t)')$, then $x_i(t)'$ is considered the elite solution at iteration t. Let x_{ij} represent the value of the individual x_i in the j th dimension, and its opposite solution is expressed as:

$$x_{ij}(t)' = m\left(l_{ij}(t) + u_{ij}(t)\right) - x_{ij}(t) \tag{14}$$

Where m is a random number between 0 and 1, referred to as the elite opposition coefficient. $l_{ij}(t)$ and $u_{ij}(t)$ represent the minimum and maximum values of $x_i(t)'$ in the j th dimension, respectively, and $\left[l_{ij}, u_{ij}\right]$ denotes the interval defined by the elite group.

4.2. Optimization target

This study integrates the root mean square error (RMSE) and curve similarity metrics, simultaneously considering the data deviations and shape differences between measured and observed values.

$$RMSE = \sqrt{\frac{1}{n}\sum_{i=1}^{n}(\widehat{y_i} - y_i)^2} \tag{15}$$

Where $\widehat{y_i}$ is the observed value and y_i denotes the actual value.

When assessing curve similarity, methods such as DTW and cosine similarity can be used to reflect the shape differences of the curves. Hookloads and torques are inherently quasi-time-series data. We regard drill bit depth as a quasi-time axis — for example, fluctuations in hookloads as the drill bit depth increases during tripping-in reflect changes in frictional forces. However, drilling speed and the discontinuity of on-site data recording may lead to irregular data sampling. To better adapt to the Fisher optimal segmentation method, the collected data are grouped into sets of 30 points, and the mean value of each group is calculated as a sample point, forming a relatively uniform grid for depth intervals. Subsequently, SG filtering is applied to smooth noise. This preprocessing preserves the overall variation trend but diminishes the performance of DTW. DTW's advantage lies in handling irregularly sampled data with phase shifts on the time axis, while the preprocessing weakens this scenario and loses details of certain time-series phase shifts. In contrast, the Hausdorff distance treats curves as unordered point sets, focusing solely on the maximum inconsistency between them. This avoids the need to account for time-series features, yielding greater robustness. The Hausdorff distance is simple to implement without requiring additional parameters, and its time complexity can be reduced to $O(nlogn)$ when using efficient methods like KD-tree search. Since SSA optimization involves numerous iterations, a lower time complexity significantly enhances computational speed. Therefore, this study adopts the Hausdorff distance (Rucklidge, 1997) to measure the maximum-minimum distance between two point sets to

evaluate their degree of similarity. For two point sets $A = \{a1, a2, \ldots, am\}$ and $B = \{b1, b2, \ldots, bn\}$ in Euclidean space, its definition is as follows:

$$H(A,B) = max[h(A,B), h(B,A)] \tag{16}$$

In the equation,

$$\begin{cases} h(A,B) = max_{a\in A}\, min_{b\in B}\|a-b\| \\ h(B,A) = max_{b\in B}\, min_{a\in A}\|b-a\| \end{cases} \tag{17}$$

Where the symbol $\|\cdot\|$ represents a distance norm defined on point sets, and the Euclidean distance is used. $h(A,B)$ represents the maximum of the shortest distances from points in A to point set B. This value is referred to as the directed Hausdorff distance from A to B. $H(A,B)$ is then defined as the maximum of the two directed Hausdorff distances $h(A,B)$ and $h(B,\ A)$. The new inversion approach constructs an objective function $f(\mu)$ by combining weighted RMSE with weighted Hausdorff distance, with its specific formulation given as:

$$f(\mu) = \alpha \cdot RMSE + (1-\alpha)\cdot H(\widehat{y}_i, y_i) \tag{18}$$

In this formulation, α is set to 0.95 to emphasize the contribution of RMSE. Future applications may adjust α based on inversion requirements to balance the weighting of deviation and geometric shape in the evaluation of simulated and actual curves.

In related studies, conventional methods often solely adopt RMSE as the objective function, primarily focusing on the overall average deviation between predicted and observed values. However, minimizing only RMSE may obscure the shape details of peaks and valleys in the calculated hookload curve that correlate with the measured hookload, due to averaging local differences. These curve shapes also reflect trends in friction factors. Thus, the use of the hybrid objective function $f(\mu)$ achieves complementarity between the Hausdorff distance and RMSE. RMSE calculates the average deviation within a wellbore section; the Hausdorff distance supplements shape preservation, preventing key peaks and valleys from being masked in pursuit of low RMSE.

4.3. Intelligent inversion model development

Establish the intelligent inversion model. Using the Fisher optimal segmentation method, the wellbore is divided into multiple segments with friction factors $\{\mu_1, \mu_2, \mu_3, \ldots, \mu_n\}$, where each sparrow individual represents the friction factor $\mu_i (i = 1, 2, 3, \ldots, n)$ for a specific depth segment. Consequently, the process of identifying optimal friction factors can be regarded as an optimization problem, with $\mu_i (i = 1, 2, 3, \ldots, n)$ as the optimization variables. This series of friction factors is integrated into the stiff-string model for analysis. This process aims to obtain the theoretical curve of hookloads or surface torques varying with well depth, comprehensively considering simulated and field data's deviations and curve similarity. The approach for the intelligent inversion method of friction factors is presented in Fig. 8.

In the optimization process, the primary task is to configure the parameters of the optimization model and update the sparrow population using the OBL strategy. Subsequently, the fitness values of all sparrows are compared to determine the optimal segmented friction factors for the current population. Then, the iteration criteria are evaluated. If the termination conditions are not satisfied, the population positions are updated according to the OBL-SSA rules, iteratively optimizing the population until the objective function value meets the predefined precision requirement or the inversion reaches the maximum number of iterations, resulting in the optimal segmented friction factors. The pseudocode for the optimization process is shown in Algorithm 2 in Appendix.

Compared with conventional strategies, the segmented inversion method proposed in this study offers significant advantages. When segmenting the wellbore, dynamic programming serves to identify segmentation points by circumventing the averaging problem while addressing the limitation posed by the single friction factor in the openhole section during coarse segmentation. During the inversion process, global optimization is employed to invert simultaneously friction factors for all well segments, while these factors become mutually coupled. The evaluation criterion comprehensively assesses all measured data, ultimately yielding a set of friction factors that best align with actual conditions. Under complex wellbore conditions, the new method enhances the calculation accuracy of friction factors through appropriate segmentation and optimization algorithms, facilitating subsequent analysis and application.

Due to challenges in isolating reaming and backreaming data, the inversion approach for multi-section friction factors is extended to alternative pipe movement phases, including pick-up, off-bottom rotation and slack-off of the drillstring. During slide drilling, the coexistence of frictional drag and weight-on-bit complicates the direct determination of friction factors. Similarly, the surface torque is the sum of bit torque and frictional torque under rotary drilling conditions. Thus, pick-up or slack-off weights and off-bottom torque measurements provide the most reliable data for drag and torque analysis. Friction factors for each subsegment are inverted following the drillstring running in the hole. Given the high similarity of well conditions during continuous operations, the obtained segmented friction factors can serve as a reference for subsequent operating conditions. Theoretically, logging data are real drilling parameters; however, in practice, their poor correlation with the rate of penetration highlights the requirement to correct the weight on bit and bit torque to enhance the reliability of drilling efficiency monitoring. In the subsequent rotating off bottom, friction factors can be real-time back calculated every 300–500 m to facilitate the calibration of weight on bit and bit torque. Neither tripping-in nor rotating off bottom conditions applies weight on bit or bit torque. During rotary drilling, torque output from the top drive system and effective weight on bit must first overcome drag and torque at the drillstring-wellbore interface before being transmitted to the bit for rock breaking. Therefore, it is reasonable to use the obtained segmented friction factors to calibrate weight on bit and bit torque. The bit torque can be calculated as follows:

$$M_{tob} = M_0 - \int \frac{C_{f2} N D_t}{2} ds \tag{19}$$

Then comparative analysis between segmented friction factors derived from trip-out and those from tripping-in and off-bottom rotation operations can reveal downhole environmental changes and provide more effective suggestions for the subsequent drilling or casing operation. The specific operational process is shown in Fig. 9.

4.4. Algorithm comparison

To evaluate the performance of OBL-SSA, the efficiency and accuracy of GA, PSO, and OBL-SSA were compared through a simple tripping-out case. After the algorithms converge stably, the best-performing algorithm is the one with faster convergence speed and a smaller objective function value. The measured hookload data from a tripping-out operation in Well Z is shown as the solid line in Fig. 10, and the hookload calculated from the

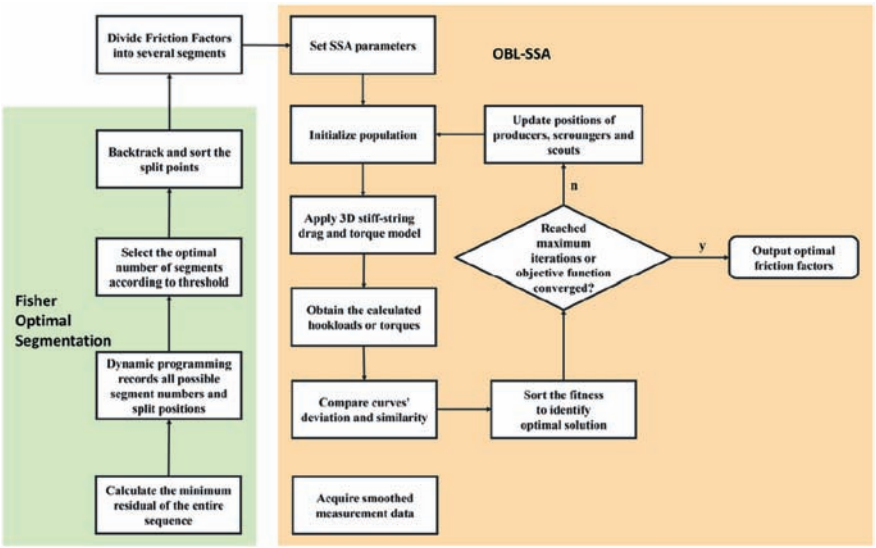


Fig. 8. Multi-Segmented inversion strategy of friction factors.

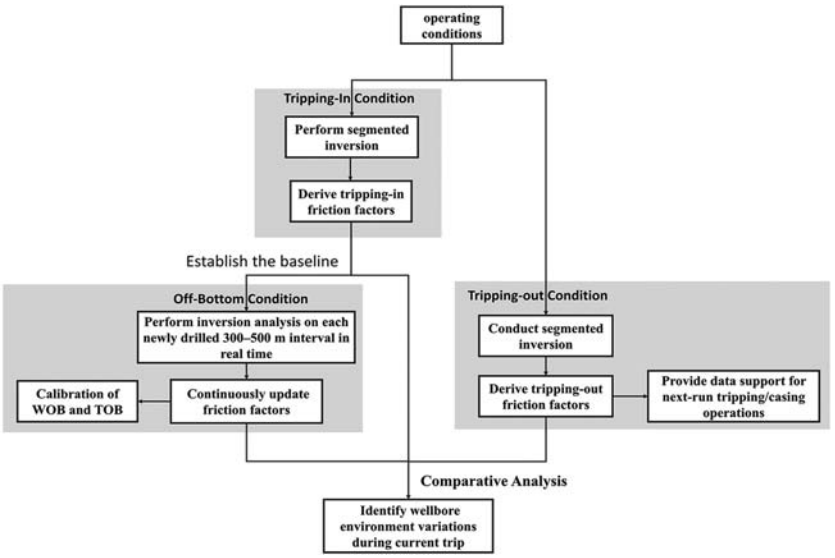


Fig. 9. Application of segmented friction factors in drilling analyses.

inversion results is plotted as the dashed line. All three algorithms ultimately converged and achieved the minimum objective function value. Among them, OBL-SSA outperformed GA and PSO with the fastest convergence speed and the smallest fitness value (see Fig. 11 and Table 3), making it the overall optimal choice in the inversion calculation for this case.

5. Case analysis

5.1. Basic data of C1 well

Logging data collected from a horizontal well C1 in the Sichuan-Chongqing region validated the proposed inversion strategy. The well was completed with a three-stage casing design. The well trajectory, wellbore structure, drillstring assembly components, and the drilling fluid parameter are summarized in Tables 4–7, respectively.

5.2. Inversion based on tripping-in

5.2.1. Selection of tripping-in hookloads

This case is based on measured hookloads during tripping-in from the wellhead to a depth of 3911 m from 08:56:36 on August 19, 2022 to 06:54:27 on August 20, 2022. Savitzky-Golay filtering was applied to reduce noise. Calculated hookload curves were simulated under distinct friction factors. The raw data, filtered data, and simulation results are presented in Fig. 12. Since hookloads in the casedhole show a linear trend, the friction factor requires no segmentation and is assumed constant. This study focuses on analyzing the openhole section.

5.2.2. Well section segmentation

The Fisher optimal segmentation method was employed to identify the measured hookload curves of the openhole section, with the *Threshold* set to 0.85. The curve segmentation results are

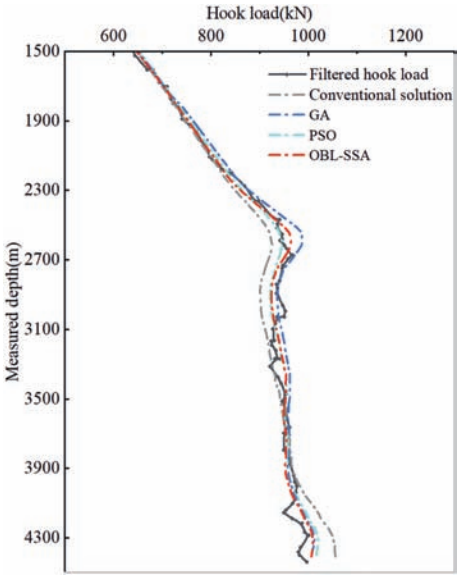


Fig. 10. Comparative inversion results of different algorithms.

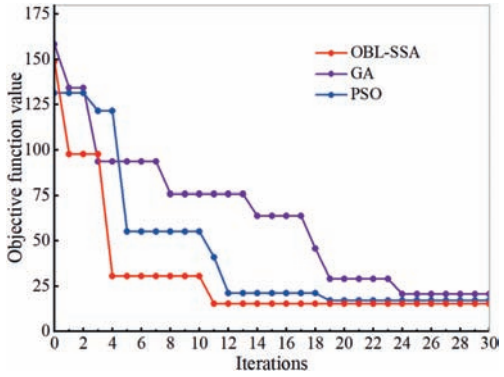


Fig. 11. Convergence curve of the three algorithms.

shown in Fig. 13. Friction factors were assigned to each well segment, as presented in Table 8.

5.2.3. Parameter settings of SSA

Before conducting friction factor inversion, accurately setting the model parameters is critical. This not only ensures the reliability of the results but also accelerates the model's convergence to an optimal solution. The friction factor may vary depending on the wellbore section type. Friction factors are lower in the cased section due to smoother wellbore walls and enhanced mud circulation, but higher in the open-hole section. The bounds for the friction factor are set to $[0.10, 0.60]$ based on field experience from drilling operations, which aligns well with actual on-site conditions. Notably, the segmented friction factors calculation method in this paper applies to conventional conditions without sticking incidents or significant manual interventions. For instance, sticking accidents should be assessed by comparing measured and theoretical hookloads, rather than relying solely on inversion. An excessively large range will significantly reduce SSA's optimization speed, while an overly small range will cause large deviations between optimization results and actual values. The $[0.10, 0.60]$ range is set to balance optimization efficiency and result accuracy.

In the SSA, the population size for small-scale problems is typically set between 10 and 30 to balance search space diversity with rapid convergence. For complex large-scale problems, the population size is typically increased to above 100. The proportion of producers is typically set between 10% and 30%, while the remaining sparrows are classified as scroungers. The configuration of producers and scroungers significantly affects the algorithm's stability. Increasing the number of producers boosts exploration but may lead to local optima, whereas more scroungers improve global search but slow convergence. The proportion of sentinels detecting potential danger typically ranges from 10% to 20% in a sparrow population. These sentinels are randomly selected. The safety threshold, reflecting sparrows' sensitivity to environmental risks, is typically set between 0.6 and 0.8. To accelerate the inversion, initial values can be derived from the conventional method of general segmentation. Parameter settings are presented in Table 9.

Table 3
Optimization results.

Algorithm	The minimum of the objective function	Hausdorff distance	RMSE
OBL-SSA	15.338	41.39	13.97
GA	20.677	47.31	19.27
PSO	16.972	46.91	15.39

Table 4
The well trajectory of well C1.

Measured depth [m]	Inclination [∘]	Azimuth [∘]
0.00	0.00	0.00
14.52	4.03	247.79
… …	… …	… …
1445.09	8.5	96.71
1465.57	8.17	96.16
1494.26	9.31	97.2
… …	… …	… …
4378.04	96.2	8.65
4406.8	94.35	8.94
4435.57	93.54	9.02
4450	93.54	9.02

Table 5
The wellbore structure of well C1.

Drilling sequence	well depth [m]	Bit size [mm]	Casing size [mm]
1	675	406.4	339.7
2	2366	311.2	244.5
3	4515	215.9	127

Table 6
Partial components of drillstring assembly in the 8½-in. section.

Tool	OD [mm]	ID [mm]	Length [m]	Cumulative Length [m]	Weight/Length [N/m]
NMDP	127	76.2	9.48	9.48	490
HWDP	127	76.2	133.19	142.67	686
DP	127	108.6	86.51	229.18	284.3
DP	127	101.6	1958.87	2188.05	373.3
DP	139.7	121.4	2279.04	4467.09	319.4

Table 7
Drilling fluid parameter.

Density [g/cm^3]	φ3	φ6	φ100	φ200	φ300	φ600
1.98	5	6	35	58	79	140

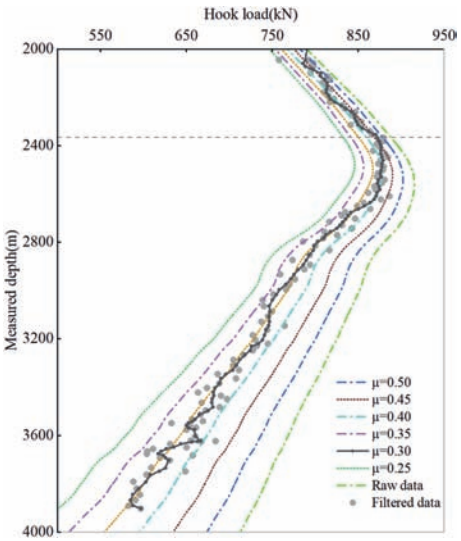


Fig. 12. Actual vs. simulated hookloads with different friction factors in trip-in operation.

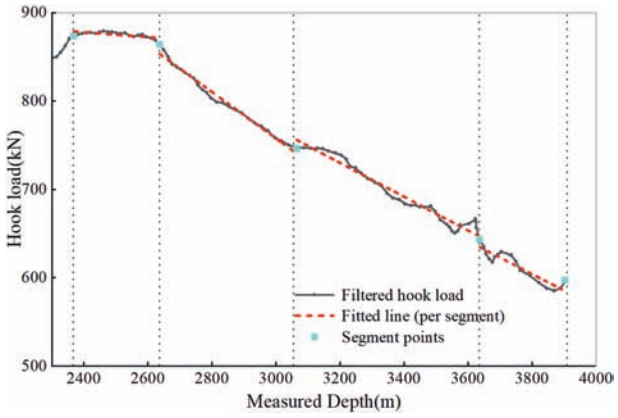


Fig. 13. Hookload curve segmentation in trip-in operation.

In general applications, the algorithm initializes population positions randomly within bounds. To boost optimization efficiency, however, this paper bases the initial population on inversion friction factors from traditional open-hole sections: five individuals are set to these inverted values, while the rest remain random. This multi-start approach accelerates convergence to true values, enhancing both computational efficiency and result accuracy.

5.2.4. Inversion of friction factors

The intermediate casing shoe depth is 2366 m, according to Well C1's logging data. Friction factors were analyzed separately for cased and openhole sections using the conventional method of general segmentation. Inversion results show friction factors of 0.26 for the cased and 0.35 for the openhole section, as depicted by the blue curve in Fig. 14, with the deviations relative to measured data represented by the cyan shade area.

Table 9
Parameter settings.

SSA Parameters	Parameter Value
Population Size	20
Iteration	30
Producer Dimension (*PD*)	20%
Security Dimension (*SD*)	10%
Safety Threshold (*ST*)	0.8
Friction Factor	[0.10–0.60]

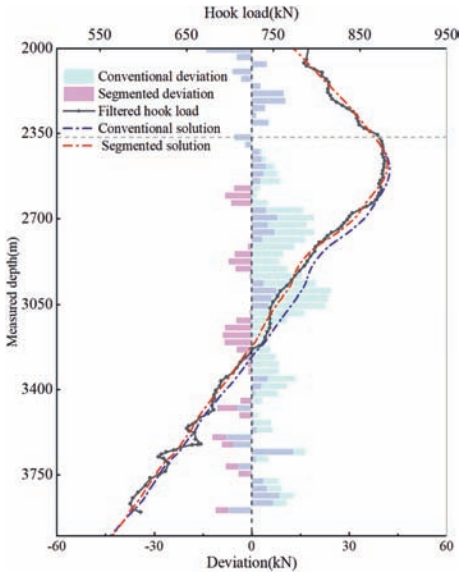


Fig. 14. Conventional vs. multi-segmented inversion calculation results in trip-in operation.

The SSA enables the inversion model to extensively search for the optimal solution in the solution space. Sparrow population values vary during iterations due to parameter differences, theoretically converging toward the optimal solution. For Well C1, intelligent inversion with iterative optimization minimized errors between simulated and measured hookloads, identifying final friction factors as the global optimum. Table 10 presents the inversion of multi-section friction factors. Hookloads calculated from the multi-section inversion results are depicted by the red curve in Fig. 14, with the error represented by the purple shaded area. The iteration process is shown in Fig. 15. The optimal objective function value is 6.921, with an RMSE of 6.195 kN m and a Hausdorff Distance of 20.721.

Fig. 14 demonstrates that hookloads derived from the multi-section friction factor inversion align more closely with the

Table 8
Segmentation results of well sections in trip-in operation.

No.	Well sections [m]	Friction factors
1	0–2366	μ_1
2	2366–2636	μ_2
3	2636–3054	μ_3
4	3054–3635	μ_4
5	3635–3911	μ_5

Table 10
Inversion results of segmented friction factors in trip-in operation.

No.	Well sections [m]	Friction factors
1	0–2366	0.26
2	2366–2636	0.45
3	2636–3054	0.40
4	3054–3635	0.29
5	3635–3911	0.33

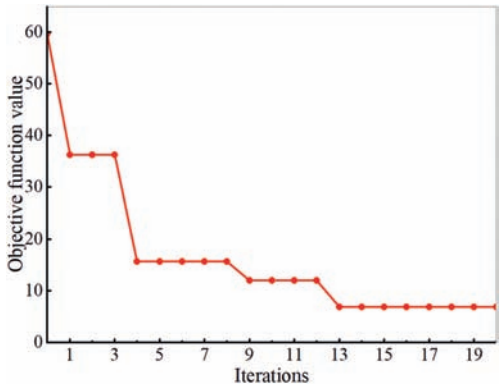


Fig. 15. Change of objective function value during iterations in trip-in operation.

Table 11
Error analysis for each well segment during trip-in.

Well section [m]	Conventional solution			Segmented solution		
	Friction factor	MAE [kN·m]	MAPE [%]	Friction factors	MAE [kN·m]	MAPE [%]
0–2366	0.26	\	\	0.26	\	\
2366–2636	0.35	4.41	0.50	0.45	4.43	0.51
2636–3054	0.35	15.83	2.00	0.40	5.18	0.65
3054–3635	0.35	8.79	1.25	0.29	5.27	0.76
3635–3911	0.35	8.34	1.36	0.33	6.70	1.10

trend of the measured curve. Our study employs MAE and MAPE as evaluation metrics to compare both methods' accuracy. The hookload curve obtained from the multi-section method yields an overall MAE of 5.14 kN m and a MAPE of 0.71% compared to the measured curve, significantly outperforming the conventional inversion results of 9.40 kN m and 1.28%. Specific segment errors are detailed in Table 11.

5.3. Inversion based on off-bottom rotating

5.3.1. Selection of off-bottom rotating surface torque data

This case collected data under the off-bottom rotating condition from a depth of 3911 m at 07:35:44 on August 20, 2022–4515 m at 11:38:27 on August 23, 2022. As shown in Fig. 16, the initial torque is represented by light gray dots, yielding the dark gray curve after Savitzky-Golay filtering. Surface torque curves simulated under different friction factors are also presented, consistent with the measured torque trend.

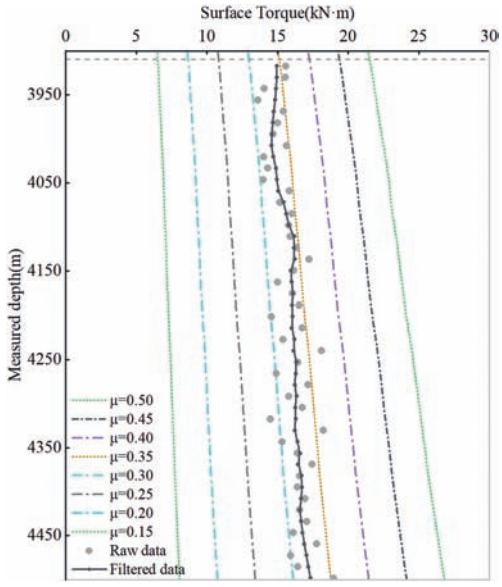


Fig. 16. Actual vs. simulated torque with different friction factors in off-bottom operation.

Table 12
Segmentation results of well sections in off-bottom operation.

No.	Well sections [m]	Friction factors
1	3911–4211	μ_1
2	4211–4515	μ_2

Table 13
Inversion results of segmented friction factors in off-bottom operation.

No.	Well sections [m]	Friction factors
1	3911–4211	0.29
2	4211–4515	0.26

5.3.2. Setting the real-time inversion depth interval

Drilling is conducted intermittently throughout the drilling process with each drilling phase covering only a portion of the wellbore, unlike tripping conditions that encompass the entire wellbore in a single operation. Since the multi-section inversion requires measured data of the entire wellbore, it is challenging to apply directly to off-bottom rotation. However, since friction factors vary dynamically, shorter time intervals enable more accurate prediction of current values. The off-bottom rotation phase immediately followed the tripping-in operation described above, allowing friction factors derived from tripping-in to serve as the basis for modeling conditions prior to a depth of 3911 m. This study aims to perform real-time segmented inversion of friction factors to calibrate bit torque and weight on bit. Given the requirement of complete torque data by the Fisher optimal segmentation method, this study employs equidistant segmented inversion with adjustable intervals based on specific requirements in place of the Fisher optimal segmentation method. This case targeted a drilling depth of 4515 m with friction factor inversion conducted at every 300-m interval. Corresponding friction factors are listed in Table 12.

5.3.3. Inversion of friction factors

Using the general segmented inversion method, the wellbore is divided into two segments, 0 m–2366 m and 2366 m–4515 m for

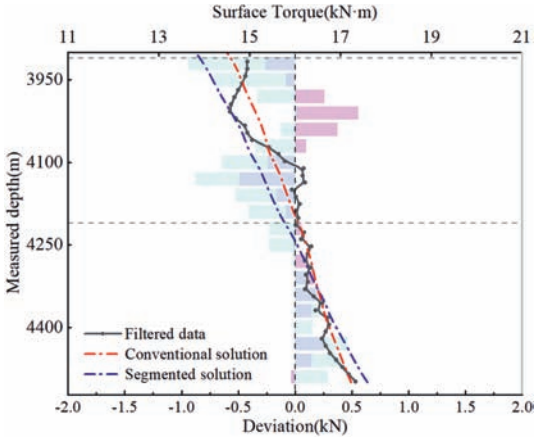


Fig. 17. Conventional vs. multi-segmented inversion calculation results in off-bottom operation.

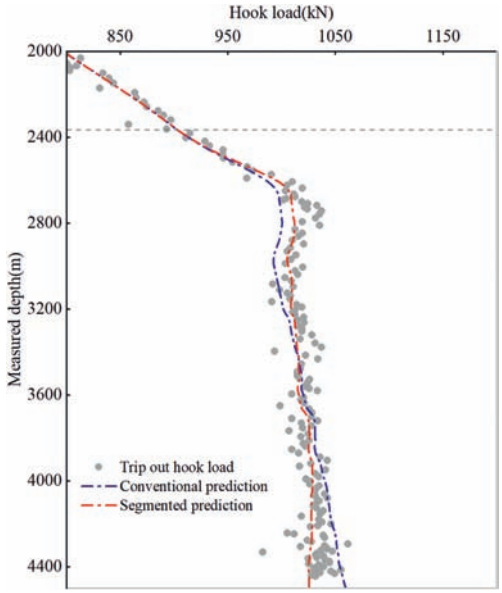


Fig. 18. Prediction of trip-out hookloads.

inversion. The results indicate a friction factor of 0.26 for the casing section and a friction factor of 0.34 for the openhole section, providing the simulated surface torque curve that best matches the measured curve. Parameters are back calculated every 300 m using the SSA to determine a set of friction factors that minimize the objective function value. After inverting the friction factor for the 3911 m–4211 m segment, bit torque and weight on bit in this segment can be calibrated, and then the subsequent segment was analyzed. Final results are presented in Table 13. As shown in Fig. 17, the blue curve represents the torque simulated by the conventional method of general segmentation, while the red curve depicts the torque derived from real-time segmented inversion.

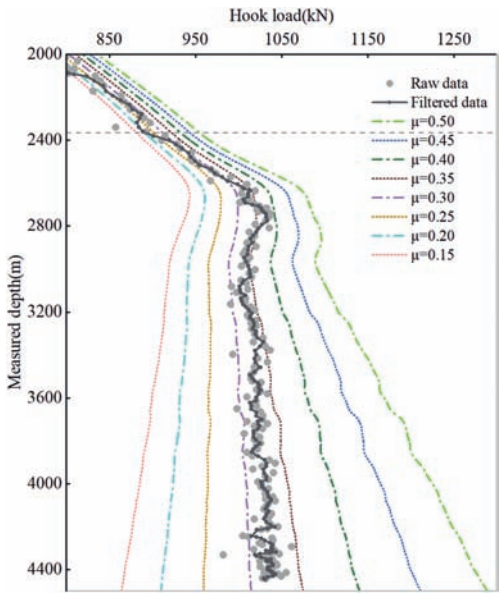


Fig. 19. Actual vs. simulated hook load with different friction factors in trip-out operation.

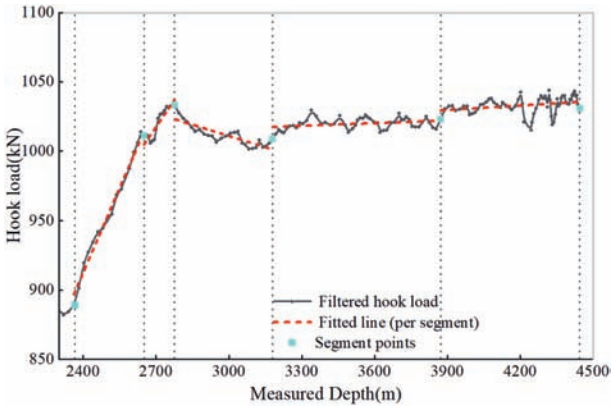


Fig. 20. Hook load curve segmentation in trip-out operation.

5.4. Prediction of trip-out hookloads based on trip-in and off-bottom friction factors

Multi-section friction factors derived from tripping-in and off-bottom rotation inversion can be used to predict tripping-out hookloads. To verify the prediction accuracy, this study collected hookloads from Well C1 during the subsequent tripping-out phase. Logging data indicate that the tripping started at a depth of 4445 m at 14:36:59 on August 23, 2022, and reached the wellhead at 09:31:24 on August 24, 2022. Raw measured data and predicted results are shown in Fig. 18. The results demonstrate that the multi-segmented inversion yields higher reliability.

5.5. Inversion based on tripping-out

5.5.1. Selection of tripping-out hookloads

The POOH hookloads from Section 5.4 were filtered using the Savitzky-Golay method, with Fig. 19 simultaneously depicting hookload curves under different friction factors.

5.5.2. Well section segmentation

The hookload curve for the openhole section was analyzed in the tripping out process. The *Threshold* for the Fisher optimal segmentation method was set to 0.80. Fig. 20 illustrates the complete segmentation results of the curve, with friction factors for each segment listed in Table 14.

5.5.3. Inversion of friction factors

Consistent with the previous case, the study first employed the conventional solution of general segmentation. Calculations indicate that a friction factor of 0.26 for the cased and 0.36 for the openhole section yield simulated hookloads most closely matching the measured pick-up weights, as shown by the blue curve in Fig. 21.

The SSA parameter settings in this section are identical to those in Section 5.2.3. A set of friction factors minimizing the objective

Table 14
Segmentation results of well sections in trip-out operation.

No.	Well sections [m]	Friction factors
1	0–2366	μ_1
2	2366–2650	μ_2
3	2650–2776	μ_3
4	2776–3179	μ_4
5	3179–3872	μ_5
6	3872–4445	μ_6

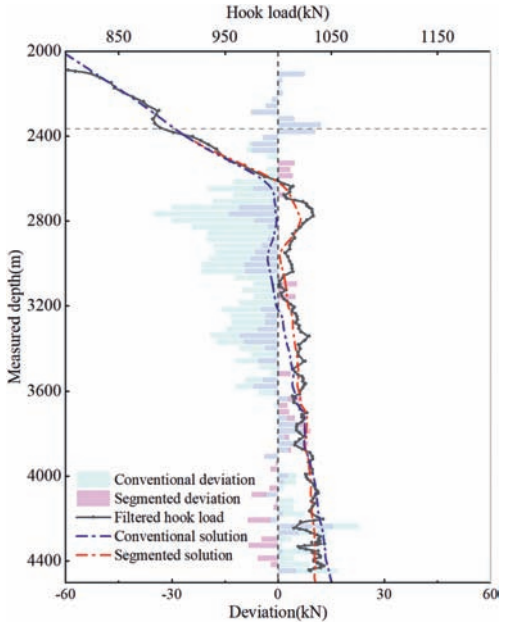


Fig. 21. Conventional vs. multi-segmented inversion calculation results in trip-out operation.

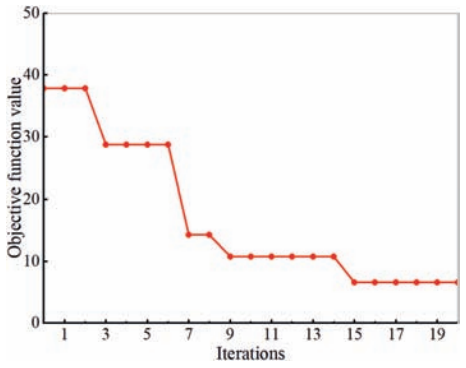


Fig. 22. Change of objective function value during iterations in trip-out operation.

function value was ultimately obtained. In Fig. 21, the red curve depicts the hookload calculated using the multi-segment inversion method. Fig. 22 illustrates the convergence history of the objective function optimization process, achieving a final objective function value of 6.560. At this point, the RMSE is 6.052 kN m, and the Hausdorff distance is 16.209. Table 15 summarizes the inversion results for segmented friction factors.

The MAE between the hookload curve simulated by the conventional method and the measured values is 10.81 kN m, with an MAPE of 1.07%. Meanwhile, the new solution demonstrates significantly improved accuracy, with an MAE of just 4.90 kN m and an MAPE of 0.49%. A detailed comparison of the MAE and MAPE for each segment between these two approaches is provided in Table 16. Based on the MAE error data from 9 wellbore sections divided in trip-in and trip-out operations in Well C1, this study employs the Wilcoxon signed-rank test to verify whether there is a significant difference between the results of the two approaches. The calculation results show a p-value of 0.0078 (<0.05), confirming that the MAE of the optimized results in Well C1 is significantly lower than that of the traditional results. The Wilcoxon test can initially verify the significance for single-well

Table 15
Inversion results of segmented friction factors in trip-out operation.

No.	Well sections [m]	Friction factors
1	0–2366	0.26
2	2366–2650	0.45
3	2650–2776	0.49
4	2776–3179	0.32
5	3179–3872	0.31
6	3872–4445	0.29

Table 16
Error analysis for each well segment during trip-out.

Well section [m]	Conventional solution			Segmented solution		
	Friction factor	MAE [kN·m]	MAPE [%]	Friction factors	MAE [kN·m]	MAPE [%]
0–2366	0.26	\	\	0.26	\	\
2366–2650	0.36	8.91	0.92	0.45	6.22	0.66
2650–2776	0.36	23.22	2.27	0.49	7.62	0.74
2776–3179	0.36	17.45	1.72	0.32	5.12	0.51
3179–3872	0.36	8.67	0.85	0.31	5.05	0.50
3872–4445	0.36	6.31	0.61	0.28	4.57	0.44

results, while the *t*-test will further assess the robustness of cross-well results. Future research will expand to multi-well datasets, employing significance testing to validate the reliability of the accuracy improvements.

Compared to the tripping-in results in Section 5.2, friction factors in the build-up section during tripping operations are consistently greater than 0.4, with even higher values exceeding 0.45 while pulling out of the hole. This difference may occur because, unlike in horizontal sections where friction factors are similar due to consistent contact, the drillstring-wellbore contact behavior differs significantly between tripping-in and tripping-out in the build-up section. In curved intervals, a tensioned drillstring generates additional side forces against the wellbore wall, resulting in greater lateral stress during tripping-out through the build-up section compared to tripping-in, thereby increasing the drag. Furthermore, increased hookloads in this interval may also result from wellbore curvature. Wellbore curvature may lead to inefficient hole cleaning or borehole stability during tripping-out, leading to cuttings buildup and higher drag.

The high drag serves as a critical indicator, signaling the need for proactive measures. Analysis of the previous operation provides recommendations for the subsequent drilling or casing running operations. For instance, if tripping-out difficulties are assessed, backreaming should be implemented to break up cuttings beds and gradually transport cuttings to the surface. This process requires vigilance against cuttings accumulation to prevent annular blockage and pressure buildup, which may lead to lost circulation. Additionally, when running casing, push-down tools should be prepared in advance, or floating casing techniques can be adopted to mitigate the impact of high drag during casing deployment. For casing running, push-down tools should be prepared in advance, or partial floatation technology should be adopted to reduce the impact of high drag.

5.6. Challenges and prospects

Accurate determination of friction factors is fundamentally constrained by measured data quality. For the Fisher optimal segmentation algorithm, noise amplifies local data fluctuations, leading to distorted RSS calculations. The algorithm may misidentify noise as sudden changes in friction, which invalidates

its original purpose of grouping wellbore sections with similar friction characteristics into the same unit. For SSA, noise distorts the input basis of the optimization function, directing the algorithm toward erroneous search directions. This reduces convergence speed, increases the probability of falling into local optima, and ultimately hinders the accurate identification of true results.Missing data directly affects segmentation and inversion. Long missing data segments render the corresponding sections ineligible for both segmentation and inversion. Although sparse data in a certain section does not completely eliminate the possibility of segmentation, it significantly reduces the algorithm's probability of segmenting that section—this is because only sparse residual values can be compared. As the foundation for subsequent depth-based inversion, such sparse data directly impairs the inversion accuracy in subsequent wellbore sections.

To address the issues, the following preprocessing methods can be explored in subsequent studies. Before filtering, outlier removal can be performed in advance using the IQR or Z-score method. For noise in the raw data, the SG filter can adaptively adjust the window size based on the signal-to-noise ratio (SNR) with a fixed window as the basis, optimizing the filtering effect. For non-stationary noise in certain wellbore sections, the wavelet denoising method can be further adopted to better preserve the local characteristics of real hookload/torque sudden changes.

For missing data, preprocessing can be performed by referencing adjacent wells. Data from the adjacent well with the most similar trajectory and formation characteristics should be selected, and the Pearson correlation coefficient should be used to calculate the similarity of hookload/torque curves between the adjacent well and the target well outside the missing section. The missing section of the target well is subjected to cubic spline interpolation using its own valid data to generate initially interpolated data; meanwhile, interpolation is performed for the corresponding depth section of the adjacent well, and the offset value between the adjacent well and this initial interpolated result is calculated. Subsequently, the target well's supplemented curve is weighted and fused with the offset value, with the weight ratio positively correlated with the similarity. It is required that the Pearson correlation coefficient between the fully supplemented data of the target well and the adjacent well's data is not lower than the original value; if this requirement is not met, the weights are adjusted for recalculation.

The inversion process involves optimization of multiple friction factors, constituting a complex multimodal optimization problem that may increase the convergence time of SSA in finding the global optimum. Although OBL has been introduced to enhance global search capability, the risk of converging to local optima remains. Multi-start optimization and multiple parameter tuning were utilized to address this issue to achieve satisfactory results. Each objective function evaluation during iterations requires calculations using the drag and torque model, resulting in high computational costs. Employing a more optimized model is recommended to reduce the total inversion time.

Future work could implement the following improvements to enhance the robustness of this method. Bayesian optimization and other adaptive search strategies could be adopted, or neural networks could be integrated to improve the accuracy and stability of the SSA. Surrogate models could be introduced to approximate the iterative calculations of the calculation model, thus minimizing computational overhead. Additionally, multi-objective optimization methods could be incorporated to simultaneously optimize the simulation accuracy of surface torques and hookloads, ultimately enhancing the reliability of inversion results.

6. Conclusions

(1) This paper proposes a multi-section friction factor inversion method based on the morphological characteristics of real drilling data curves. By integrating the Fisher optimal segmentation method with OBL-SSA, optimal segmented friction factors are derived, providing data support for analyzing the drag and torque in subsequent drilling operations.
(2) Multi-section friction factors overcome the limitations of conventional methods, such as the averaging problem and neglecting local drag details. Calculation results exhibit a stronger correlation with measured data. In the case of Well C1, the MAE of the segmented inversion for tripping-in and tripping-out operations is reduced by approximately 50% compared with conventional methods, and the Wilcoxon test yields a p-value of 0.0078 (<0.05). This confirms that the new method achieves significantly higher accuracy than the traditional method for Well C1. Future work can be extended to multi-well cases, where the robustness of accuracy improvements can be analyzed through significance tests to provide more substantial support for the reliability of the new scheme.
(3) This new method can be applied to the tripping-in, off-bottom rotation, and tripping-out phases during operations. Friction factors are back-calculated during running in hole, providing a data foundation for real-time inversion in the off-bottom rotation operation. This enables optimization of weight on bit and bit torque. Inversion results from tripping-in and off-bottom rotation can be compared to those from the tripping-out phase, achieving a precise evaluation of the entire drilling process.
(4) The quality of measured data significantly impacts segmentation and inversion results. To enhance the reliability of results, it is recommended that high-precision measurement instruments be employed in practical applications to collect more accurate hookloads and surface torques.

CRediT authorship contribution statement

Hu Yin: Funding acquisition, Data curation. **Qianyi Xia:** Writing – original draft, Conceptualization. **Qiang Wei:** Resources. **Xiuwen Zhao:** Software, Project administration. **Qian Li:** Project administration, Funding acquisition.

Declaration of competing interest

The authors declare the following financial interests/personal relationships which may be considered as potential competing interests:

Hu Yin reports financial support was provided by National Key R&D Program of China. Hu Yin reports financial support was provided by Natural Science Foundation of Sichuan, China. If there are other authors, they declare that they have no known competing financial interests or personal relationships that could have appeared to influence the work reported in this paper.

Acknowledgments

This work was supported by the National Science and Technology Major Project (2025ZD1405900), and the Natural Science Foundation of Sichuan, China (2024NSFSC0205) and the National Key R&D Program of China (2019YFA0708302).

Appendix A. Supplementary data

Supplementary data to this article can be found online at https://doi.org/10.1016/j.ptlrs.2026.01.008.

References

Aadnoy, B.S., Fazaelizadeh, M., Hareland, G., 2010. A 3D analytical model for wellbore friction. J. Can. Pet. Technol. 49 (10), 25–36. https://doi.org/10.2118/141515-PA. SPE-141515-PA.

Carpenter, C., 2021. Digital transformation enables automated real-time torque-and-drag modeling. J. Petrol. Technol. 73 (1), 69–70. https://doi.org/10.2118/0121-0069-JPT. SPE-0121-0069-JPT.

Chen, P., Gao, D., Wang, Z., Huang, W., 2015. Study on multi-segment friction factors inversion in extended-reach well based on an enhanced PSO model. J. Nat. Gas Sci. Eng. 27, 1780–1787. https://doi.org/10.1016/j.jngse.2015.11.001.

Chi, Y., Kemajou, V., Rajan, A., Samuel, R., 2023. Cloud-based real-time well engineering: coupling torque-and-drag and uncertainty modeling. In: SPE/IADC Drilling Conference and Exhibition. https://doi.org/10.2118/212476-MS. Stavanger. SPE-212476-MS.

Craig, S.H., 2003. A multi-well review of coiled tubing force matching. In: SPE/ICoTA Coiled Tubing Conference and Exhibition. https://doi.org/10.2118/81715-MS. Houston, Texas, USA. SPE-81715-MS.

Dao, N.H., Mahjoub, M., Menand, S., Nguyen, K., 2023. Modeling of a detailed bow spring centralizer description in stiff-string torque and drag calculation. Geoenergy Sci. Eng. 222, 211457. https://doi.org/10.1016/j.geoen.2023.211457.

Fisher, W.D., 1958. On grouping for maximum homogeneity. J. Am. Stat. Assoc. 53 (284), 789–798. https://doi.org/10.1080/01621459.1958.10501479.

Gharehchopogh, F.S., Namazi, M., Ebrahimi, L., Abdollahzadeh, B., 2023. Advances in sparrow search algorithm: a comprehensive survey. Arch. Comput. Methods Eng. 30 (1), 427–455. https://doi.org/10.1007/s11831-022-09804-w.

Hareland, G., Wu, A., Lei, L., 2014. The field tests for measurement of Downhole Weight on Bit (DWOB) and the calibration of a real-time DWOB model. In: International Petroleum Technology Conference. Doha, Qatar. https://doi.org/10.2523/IPTC-17503-MS.

Ho, H.S., 1988. An improved modeling program for computing the torque and drag in directional and deep Wells. In: SPE Annual Technical Conference and Exhibition. https://doi.org/10.2118/18047-MS. Houston, Texas, USA. SPE-18047-MS.

Johancsik, C.A., Friesen, D.B., Dawson, R., 1984. Torque and drag in directional wells-prediction and measurement. J. Petrol. Technol. 36 (6), 987–992. https://doi.org/10.2118/11380-PA. SPE-11380-PA.

Lai, S.W., Wood, M.J., Eddy, A.J., Holt, T.L., Bloom, M.R., 2016. Stick/slip detection and friction-factor testing with surface-based torque and tension measurements. SPE Drill. Complet. 31 (2), 119–133. https://doi.org/10.2118/170624-PA. SPE-170624-PA.

Lindberg, M.B., 1990. Fisher: a turbo pascal unit for optimal partitions. Comput. Geosci. 16 (5), 717–732. https://doi.org/10.1016/0098-3004(90)90029-S.

Mayouf, M., Hadjadj, A., 2024. Real-time torque and drag prediction in oilwell drilling: a comparative study of machine learning models. In: International Conference on Artificial Intelligence and its Applications in the Age of Digital Transformation. https://doi.org/10.1007/978-3-031-71426-9_10. Nouakchott, Mauritania.

Mirhaj, S.A., Kaarstad, E., Aadnoy, B.S., 2016. Torque and drag modeling: soft-string versus stiff-string models. In: SPE/IADC Middle East Drilling Technology Conference and Exhibition. https://doi.org/10.2118/178197-MS. Abu Dhabi, UAE. SPE-178197-MS.

Mitchell, R.F., Samuel, R., 2009. How good is the torque/drag model? SPE Drill. Complet. 24 (1), 62–71. https://doi.org/10.2118/105068-PA. SPE-105068-PA.

Qin, L., Dong, G.C., Guo, J.X., Wei, L., Li, Z., Chen, Z., 2022. Analysis and application of horizontal well extension limit based on sectional friction factor. J. Northwest. Polytech. Univ. 46 (2), 107–116. https://xuebao.nepu.edu.cn/info/1402/10215.htm.

Rucklidge, W.J., 1997. Efficiently locating objects using the Hausdorff distance. Int. J. Comput. Vis. 24, 251–270. https://doi.org/10.1023/A:1007975324482.

Samuel, R., 2010. Friction factors: what are they for torque, drag, vibration, bottom hole assembly and transient surge/swab analyses?. In: IADC/SPE Drilling Conference and Exhibition https://doi.org/10.2118/128059-MS New Orleans, Louisiana, USA. SPE-128059-MS.

Samuel, R., Kumar, K., 2023. Real-time well engineering: String (Drillstring/Casing/Completion) runnability monitor while drilling. In: SPE/IADC Middle East Drilling Technology Conference and Exhibition. https://doi.org/10.2118/214615-MS. Abu Dhabi, UAE. SPE-214615-MS.

Savitzky, A., Golay, M.J., 1964. Smoothing and differentiation of data by simplified least squares procedures. Anal. Chem. 36 (8), 1627–1639. https://pubs.acs.org/doi/abs/10.1021/ac60214a047.

Sheppard, M.C., Wick, C., Burgess, T., 1987. Designing well paths to reduce drag and torque. SPE Drill. Eng. 2 (4), 344–350. https://doi.org/10.2118/15463-PA. SPE-15463-PA.

Tahmeen, M., Hareland, G., Aadnoy, B.S., 2014. Real-time software to estimate friction coefficient and downhole weight on bit during drilling of horizontal Wells. In: International Conference on Offshore Mechanics and Arctic Engineering. https://doi.org/10.1115/OMAE2014-24620. San Francisco, California, USA.

Tang, H., Sun, M., Feng, G., Yang, C., 2016. A monitoring method for torque & drag of extended reach Wells. Nat. Gas. Ind. 36 (5), 81–86. https://en.cnki.com.cn/Article_en/CJFDTOTAL-TRQG201605019.htm.

Tikhonov, V., Valiullin, K., Nurgaleev, A., Ring, L., Gandikota, R., Chaguine, P., Cheatham, C., 2014. Dynamic model for stiff-string torque and drag. SPE Drill. Complet. 29 (3), 279–294. https://doi.org/10.2118/163566-PA. SPE-163566-PA.

Tizhoosh, H.R., 2005. Opposition-based learning: a new scheme for machine intelligence. In: International Conference on Computational Intelligence for Modelling, Control and Automation and International Conference on Intelligent Agents, Web Technologies and Internet Commerce. https://doi.org/10.1109/CIMCA.2005.1631345. Vienna, Austria.

Wiktorski, E., Sui, D., Khalifeh, M., Khatibi, M., 2020. Investigation of the combined effects of temperature and large-scale tortuosity on friction-factor profile in straight inclined sections. SPE J. 25 (3), 1174–1192. https://doi.org/10.2118/198897-PA. SPE-198897-PA.

Xue, J., Shen, B., 2020. A novel swarm intelligence optimization approach: sparrow search algorithm. Syst. Sci. Control Eng. 8 (1), 22–34. https://doi.org/10.1080/21642583.2019.1708830.

Zhao, J., Huang, W., Gao, D., 2022. Research on dynamic prediction of tubular extension limit and operation risk in extended-reach drilling. J. Nat. Gas Sci. Eng. 107, 104542. https://doi.org/10.1016/j.jngse.2022.104542.

Zhao, J., Huang, W., Gao, D., 2024. Interaction between pipe rotation and cuttings transport in extended-reach drilling: mechanism, model, and applications. SPE J. 29 (6), 2857–2876. https://doi.org/10.2118/219483-PA. SPE-219483-PA.

Zhu, S., Song, X., Li, G., Zhu, Z., Yao, X., 2021. Intelligent real-time analysis of drill string frictional torque and sticking trend prediction. Oil. Drill. Prod. Tech. 43 (4), 428–435. https://www.cnki.com.cn/Article/CJFDTotal-SYZC202104003.htm.